PHYSICAL REVIEW E VOLUME 61, NUMBER 1 JANUARY 2000

Laser ray tracing and power deposition on an unstructured three-dimensional grid

Thomas B. Kaiser
Lawrence Livermore National Laboratory, University of California, Livermore, California 94550

(Received 30 June 1999)

A scheme is presented for laser beam evolution and power deposition on three-dimensional unstructured grids composed of hexahedra, prisms, pyramids, and tetrahedra. The geometrical-optics approximation to the electromagnetic wave equation is used to follow propagation of a collection of discrete rays used to represent the beam(s). Ray trajectory equations are integrated using a method that is second order in time, exact for a constant electron-density gradient, and capable of dealing with density discontinuities that arise in certain hydrodynamics formulations. Power deposition by inverse-bremsstrahlung is modeled with a scheme based on Gaussian quadrature to accommodate a deposition rate whose spatial variation is highly nonuniform. Comparisons with analytic results are given for a density ramp in three dimensions, and a ''quadratic-well'' density trough in two dimensions.

PACS number(s): 02.70.$-$c, 07.05.Tp, 02.60.Cb, 02.60.Lj

I. INTRODUCTION

The most highly developed energy source used to drive inertial-confinement fusion (ICF) experiments today is laser light. The current generation of computer codes used to model such experiments typically use three-dimensional (3D) unstructured grids [1–4] and may employ either finite-element, finite-difference or hybrid representations to solve Eulerian, Lagrangian or arbitrary-Lagrange-Euler [1] forms of the hydrodynamics equations. Moreover, when finite elements are used, they may be discontinuous [1]. This level of sophistication presents challenges to any scheme used to model the interaction of laser beams with materials present in the simulation.

Part of the difficulty associated with three dimensionality is the availability of sufficient computer power, which can be addressed both by choice of hardware implementation (parallel architecture, for example) and by the choice of computation and approximation methods. The former will be discussed elsewhere, the focus of the present work being primarily algorithmic. Whatever the hardware choice, a remaining need for computational efficiency and the fact that over most of the computational domain, and for most ICF applications of interest, the medium varies slowly over the laser wavelength, leads one to choose geometrical optics with absorption as an approximate solution of the full wave equation with damping. This captures most of the physical effects of interest: refraction and power deposition and even some ponderomotive effects. Diffractive effects are neglected, but there is hope of extending the method to include them [5,6].

Given a ray-tracing approach, unstructured grids pose a problem by complicating the determination of where rays cross computational-zone interfaces, an issue for both ray propagation and power deposition. In some formulations of hydrodynamics, for example, discontinuous-finite-elements, the matter density is discontinuous at zone interfaces, which leads to singularities in the effective force governing ray propagation. Proper treatment of these singularities is crucial to accurate modeling of refraction.

In an earlier treatment [7] rotational symmetry of the propagating medium was assumed, and two-dimensional quadrilateral zones were triangulated to obtain material properties that varied linearly in the radial and axial coordinates within a zone and were continuous across zone interfaces. Azimuthal ray motion was discretized by assuming constancy of the gradient of the index of refraction during a propagation subtime step, and iterative numerical root finding used to locate interface crossings.

The present work makes no assumptions about symmetry of the medium. The faces of the three-dimensional zones can be triangular or quadrilateral and have arbitrary orientation. Rays traverse a zone in a single time step whose length is determined analytically, i.e., iteration is not necessary. Constancy of the effective force governing ray motion within a zone is assumed, but accuracy is controlled by grid resolution rather than by restricting the time step. No requirement of continuity of material properties at zone interfaces is imposed.

In Sec. II the ray equation of motion is given. Inspection shows it to be that of a unit-mass particle in the potential field $V=(c^2/2)(n_e/n_c)$ where c is the speed of light, n_e is the free-electron number density, and n_c the critical density, at which the plasma frequency is equal to the laser frequency. Thus, ray propagation is completely determined by the electron-density gradient. If the ratio of the zone size to the gradient scale length is adopted as a small parameter ϵ, variation of the electron density within a computational zone can be represented as

$$n_e(\vec{x})=\langle n_e\rangle+\langle\vec{\nabla}n_e\rangle\cdot(\vec{x}-\langle\vec{x}\rangle)+O(\epsilon^2), \tag{1}$$

where $\langle\,\rangle$ denotes a zone average. A natural approximation scheme for ray motion within a zone then emerges. In lowest order, the density in a zone is constant at its average value. The ray feels no effective force and therefore moves in a straight line. In making the transition to the next zone (where the average density is, in general, different) the ray experiences a δ-function effective force normal to the zone interface, which discontinuously changes the component of its velocity normal to the interface, i.e., the transition is governed by Snell's law. To next order the density *gradient* is constant within the zone, so the ray feels a constant force that causes it to move along a parabolic trajectory. The transition to the next zone again obeys Snell's law. In lowest order refraction occurs only at zone interfaces, while at second order a ray can refract within a zone as well. Extension to higher order is straightforward but becomes computationally expensive and would be necessary only in the presence of strongly varying density within a zone, in which case mesh refinement would probably be more economical. (If the material properties were changing on the same scale as the wavelength of light, geometrical optics would be expected to break down anyway.)

In Sec. III the general problem of determining the point of intersection of a ray with a zone face is considered. The equation of an arbitrary quadrilateral face is derived under the assumption that it be of bilinear form in the two-dimensional surface coordinates. The simpler case of a triangular face is also considered, and the inverse transformation giving the surface coordinates in terms of Cartesian coordinates derived for both cases. Substitution of the ray trajectory in the face equation determines the crossing time, and substitution of the crossing time back into the face equation at the point of intersection. The unit vector normal to the surface at the point of intersection, needed for application of Snell's law, is obtained from the gradient of the function whose level surface defines the face. Finally, a criterion independent of the face equation is given for determining whether or not a ray originating at the beam source penetrates a given boundary face.

Given a model for the power-absorption rate, it can be integrated along the ray trajectory to determine the rate at which energy is deposited in a zone. In Sec. IV this is done for the inverse-bremsstrahlung process, a case in which a strongly nonuniform absorption rate must be accommodated. Knowledge of the total unattenuated ray-energy density in a zone provides the energy density in the electromagnetic field, which gives the local laser field strength parameter, $\langle (v_{\mathrm{osc}}/v_e)^2\rangle$, required for transport coefficients and ponderomotive effects.

A laser deposition package implementing this scheme has been added to ICF modeling codes currently under development at Lawrence Livermore National Laboratory [2–4]. Test cases run with the codes to check the accuracy of ray trajectories and power deposition are given in Sec. V, and in Sec. VI results are discussed, and possible extensions of the method briefly mentioned. The geometry of nonplanar faces and computation of the laser-field energy density are treated in two appendixes.

II. RAY EQUATIONS OF MOTION

In the geometrical optics approximation [9] electromagnetic wave quantities are written in the form

$$\phi=\hat{\phi}(\vec{x},t)\exp\{i\omega[S(\vec{x})/c-t]\}, \tag{2}$$

with $\hat{\phi}$ a slowly varying amplitude and the exponential phase a large quantity. The quantities ω and c are, respectively, the light frequency and the speed of light in vacuum. Retention of the dominant terms when the form (2) is substituted into the wave equation, $[\vec{\nabla}^2-(\eta/c)^2\partial^2/\partial t^2]\phi=0$, leads to the fundamental equation of geometrical optics, $|\vec{\nabla}S|^2=\eta^2$, where η is the index of refraction, assumed to vary on a much longer spatial scale than the wavelength of the light. We further assume that $\eta(\vec{x})$ is constant on the ray-transit time scale, i.e., the medium is ''frozen'' during the time required for a typical ray to traverse the grid, although it may evolve from one time step to the next. The spatially dependent part of the phase, or *eikonal*, is related to the local wave vector $\vec{k}$ by $\vec{k}=(\omega/c)\vec{\nabla}S$. Wave fronts, surfaces of constant phase, move at the phase velocity, $\omega/|\vec{k}|=c/|\vec{\nabla}S|$, while rays, which trace out curves that are everywhere normal to wave fronts, i.e., parallel to $\vec{\nabla}S$, can be thought to progress at the group velocity, $\vec{v}=\partial\omega/\partial\vec{k}=c\vec{\nabla}S$, the velocity at which energy is transported. The equation of motion of a ray can be obtained by differentiating the group velocity with respect to time [7]:

$$\begin{aligned}\frac{d^2\vec{x}}{dt^2}&=\frac{d\vec{v}}{dt}=c\,\frac{d\vec{\nabla}S}{dt}=c(\vec{v}\cdot\vec{\nabla})(\vec{\nabla}S)=c^2(\vec{\nabla}S\cdot\vec{\nabla})(\vec{\nabla}S)\\&=\frac{c^2}{2}\vec{\nabla}(|\vec{\nabla}S|^2)=\vec{\nabla}\left(\frac{c^2}{2}\,\eta^2\right).\end{aligned} \tag{3}$$

The index of refraction, or, equivalently for transparent materials, the dielectric function, $\epsilon_D=\eta^2$, is a known function of position for a given material. In a nonrelativistic unmagnetized plasma, which for definiteness will be adopted as a model here, it is given by

$$\eta^2=1-\frac{\omega_p^2}{\omega^2}=1-\frac{n_e}{n_c}, \tag{4}$$

where ω_p is the plasma frequency, ω is the laser frequency, and $n_c=(m_e/4\pi)(\omega/e)^2$ is the critical density, at which the laser frequency and plasma frequency are equal. (The quantities m_e and e are the electron mass and charge, respectively.) Combining Eq. (4) with Eq. (3) gives the final form of the ray equation of motion:

$$\frac{d^2\vec{x}}{dt^2}=\vec{\nabla}\left(-\frac{c^2}{2}\,\frac{n_e}{n_c}\right). \tag{5}$$

Rays move as unit-mass particles in the potential $V=(c^2/2)n_e/n_c$.

Hydrodynamics codes discretize the fundamental equations on meshes of points that define computational nodes and zones. Some quantities, typically even moments of the underlying distribution function, are specified in the zones, while others, typically the odd moments, are specified at nodes. The electron density is not usually followed with an evolution equation. Rather it is reconstructed when needed from other quantities like the mass density, ionization state, mass number, material fractions, etc. In addition to $\langle n_e\rangle$, we also require $\langle\vec{\nabla}n_e\rangle$ in each zone [8] in order to integrate Eq. (5). To lowest order [in the sense of Eq. (1)] the equation of motion is $d^2\vec{x}/dt^2=0$, so that the ray crosses the zone in a straight line. To next order $d^2\vec{x}/dt^2 = -(c^2/2)\langle\vec{\nabla}n_e\rangle/n_c$, resulting in the parabolic trajectory characteristic of a constant force field.

In the approximation (1) the electron density is not, in general, continuous across the interface separating two adjacent computational zones. From Eq. (5) it is clear that this discontinuity appears in the ray equation of motion as a singularity in the component of the force normal to the interface. Thus, in passing through the interface the component of the ray velocity normal to the interface incurs a discontinuous change, while the component tangent to the interface is conserved, i.e., the ray refracts. To compute the effect of the instantaneous acceleration, let s be the distance measured along the interface normal, and $v_\perp$ the associated component of the velocity. Then in this direction, $d/dt = v_\perp \partial/\partial s$ by definition, so that the component of Eq. (5) normal to the interface can be written

$$\frac{\partial}{\partial s}\left(v_\perp^2 + \frac{n_e}{n_c}c^2\right) = 0 \Rightarrow \Delta v_\perp^2 = -\Delta\left(\frac{n_e}{n_c}c^2\right), \tag{6}$$

where $\Delta(\ \ldots\ )$ represents the change across the interface. Clearly, for a given value of $v_\perp^2$ there is a maximum density discontinuity consistent with transmission, viz., $\Delta n_e \leqslant (v_\perp^2/c^2)n_c$. For larger discontinuities Eq. (6) cannot be satisfied for a transmitted ray. In that case the ray must remain in the initial zone and the only solution of Eq. (6) is $\Delta n_e = 0$. Then, $\Delta v_\perp^2 = 0 \Rightarrow v_\perp \rightarrow -v_\perp$, i.e., the ray reflects. Note that ray reflection occurs only for sufficiently large density discontinuities, unlike the case for solutions of the full electromagnetic wave equation, where some reflection would take place for any nonvanishing density jump.

Equation (6) is consistent with Snell's law, which may be seen by noting that the effective total energy associated with motion governed by Eq. (5) is conserved:

$$\frac{1}{2}v^2 + \frac{1}{2}\frac{n_e}{n_c}c^2 = \frac{1}{2}c^2. \tag{7}$$

That is,

$$v^2 = \left(1 - \frac{n_e}{n_c}\right)c^2, \tag{8}$$

as expected [recall Eq. (4)]. Combination of Eqs. (8) and (6) verifies that the velocity component tangent to the interface is conserved, which can be expressed

$$\sqrt{1 - n_e/n_c}\,\sin\theta = \sqrt{1 - n_e'/n_c}\,\sin\theta',$$

or, with substitution from Eq. (4),

$$\eta\sin\theta = \eta'\sin\theta', \tag{9}$$

where unprimed (primed) quantities denote values before (after) the transition, and θ is the angle between the ray velocity and the interface normal. Equation (9) is the usual statement of Snell's law.

Equations (1), (3), and (9) in general, or Eqs. (1), (5), and (6) when Eq. (4) holds, provide a prescription for propagating rays through an unstructured grid. In lowest order all that is needed is the average dielectric function or electron density in each computational zone. At this level of description rays are sequences of connected straight-line segments punctuated by discontinuous changes of direction at each zone interface encountered. Although this extremely simple scheme can be adequate for highly underdense plasmas, where refractive effects are small, it can be unacceptably inaccurate near critical surfaces, where $n_e \approx n_c$. Furthermore, there are certain geometric configurations in which it fails badly. For example, consider a cylindrically symmetric density field discretized on a Cartesian grid with the z axis the axis of symmetry, and a ray traveling parallel to the x or y axis. Although the average gradient is in the radial direction, at each zone interface it is in either the x or y direction, as is, therefore, the effective force. Since rays refract only at interfaces they never feel radial forces, and thus will never undergo a transverse acceleration, and so will never refract (although reflection is possible) [10].

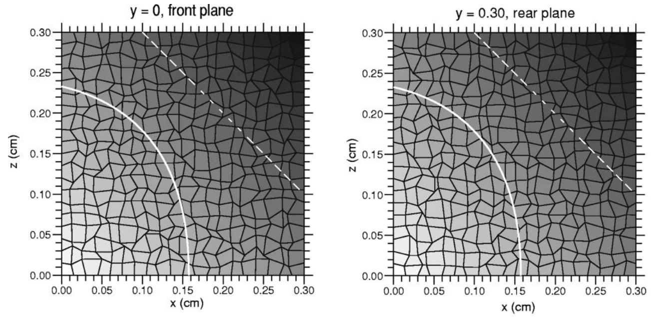

FIG. 1. Trajectory of a ray (solid white line) through a randomized three-dimensional mesh projected along with the front and rear mesh points onto a plane perpendicular to the y axis. (Notice that the projections of the front and rear faces of each zone are different.) The average electron number density in a zone, which varied from 0 on the y axis to $(3/2)n_c$ on the line $x=z=0.3$, is indicated by the gray scale. The critical surface is indicated with a dashed white line.

Retaining the average density gradient in the equation of motion overcomes this deficiency. The ray trajectory within a zone is second order in the time step, and, therefore, inherently more accurate. Whereas the lowest order trajectory is exact only in the uninteresting case of constant density, the second-order trajectory is exact in a material with constant electron-density *gradient*, which is a good local approximation given a sufficiently refined mesh. An example, discussed more fully in Sec. VI, is seen in Fig. 1, where a ray is shown propagating across a constant density gradient. If the density gradient is globally constant, there are no density discontinuities at zone interfaces, so the trajectories are smooth, i.e., continuous through first derivatives. The extent to which $\vec{\nabla}n_e$ is not globally constant determines the size of density discontinuities, which in turn determines the amount by which rays must bend discontinuously at zone interfaces to compensate for the lack of resolution in the effective force.

III. INTERSECTION OF RAYS WITH ZONE FACES

A. Equations of faces

In order to determine the point at which a ray passes from one computational zone to another the equation of the interface as a surface in three dimensions is required. Defining a zone interface as a surface bounded by straight lines (edges) that connect nodes (vertices) shared by two adjacent zones, we consider the particular cases of four edges (quadrilateral faces), and three edges (triangular faces). This makes the scheme applicable to all zone types allowed in linear-finite-element codes, viz., hexahedra, prisms, pyramids, and tetrahedra. Faces with more than four edges do not admit a bilinear spatial representation, which we want to preserve to maintain consistency with the finite-element formalism. Such faces can always be decomposed into triangular and quadrilateral ''subfaces.''

1. Quadrilateral faces

The surface containing four given points in space and the straight lines connecting them is, of course, not unique. We make it so by requiring its representation to be of bilinear form in the local surface coordinates. That is, if $\{x_i\}$, $i=1,2,3$ are Cartesian coordinates we introduce a two-dimensional (dimensionless) coordinate system in a face, $\{\alpha,\beta\}$, such that

$$x_i=a_{i0}+a_{i1}\alpha+a_{i2}\beta+a_{i3}\alpha\beta, \tag{10}$$

where

$$-1\leqslant\alpha,\beta\leqslant 1, \tag{11}$$

the extreme values corresponding to the four nodes that determine the face. In (α,β) space the face is planar and square, and the Cartesian coordinates vary linearly in each local coordinate when the other is held fixed. In Cartesian space the edges of the face are straight lines, but the face is, in general, not planar. In a bilinear finite-element representation the transformation (10) would also be used as an interpolant to evaluate numerically the integrals that typically arise in, e.g., a Galerkin formulation [11]. In that case α and β are referred to as ''isoparametric'' coordinates.

The coefficients a_{ij} are particular linear combinations of the nodal Cartesian coordinates that can be determined by substituting the four possible combinations of extreme values of α,β in Eq. (10). Specifically, if the nodes are numbered {0, 1, 2, 3}, corresponding to the cyclically ordered [12] local coordinate pairs $\{(\alpha,\beta)\}=\{(-1,-1),(-1,1),(1,1),(1,-1)\}$, and x_i^k is the ith Cartesian component of the location of node k, the collection of Eqs. (10) for the four nodes for $i=1,2,3$, when written in matrix form, can be inverted to obtain the a_{ij} coefficients:

$$\begin{pmatrix} a_{i0}\\ a_{i1}\\ a_{i2}\\ a_{i3}\end{pmatrix}=\frac{1}{4}\begin{pmatrix} 1 & 1 & 1 & 1\\ -1 & -1 & 1 & 1\\ -1 & 1 & 1 & -1\\ 1 & -1 & 1 & -1\end{pmatrix}\begin{pmatrix} x_i^0\\ x_i^1\\ x_i^2\\ x_i^3\end{pmatrix}. \tag{12}$$

Given the Cartesian coordinates of the nodes, Eq. (12) can be used to compute the coefficients in the transformation to surface coordinates: Eq. (10). The equation of the surface in Cartesian coordinates can then be obtained as follows. Let $\vec{a}_j$ be the vector whose Cartesian components are $\{a_{1j},a_{2j},a_{3j}\}$. Then Eqs. (12) can be written

$$\begin{aligned}\vec{a}_0&=(\vec{x}^0+\vec{x}^1+\vec{x}^2+\vec{x}^3)/4,\\ \vec{a}_1&=(-\vec{x}^0-\vec{x}^1+\vec{x}^2+\vec{x}^3)/4,\\ \vec{a}_2&=(-\vec{x}^0+\vec{x}^1+\vec{x}^2-\vec{x}^3)/4,\\ \vec{a}_3&=(\vec{x}^0-\vec{x}^1+\vec{x}^2-\vec{x}^3)/4,\end{aligned} \tag{13}$$

and Eq. (10) as

$$\vec{x}-\vec{a}_0=\vec{a}_1\alpha+\vec{a}_2\beta+\vec{a}_3\alpha\beta. \tag{14}$$

From Eq. (14) it follows immediately that

$$\begin{aligned}D\alpha&=(\vec{a}_2\times\vec{a}_3)\cdot(\vec{x}-\vec{a}_0),\\ D\beta&=(\vec{a}_3\times\vec{a}_1)\cdot(\vec{x}-\vec{a}_0),\\ D\alpha\beta&=(\vec{a}_1\times\vec{a}_2)\cdot(\vec{x}-\vec{a}_0),\end{aligned} \tag{15}$$

where $D\equiv\vec{a}_1\cdot(\vec{a}_2\times\vec{a}_3)$. Now, from Eqs. (13) it can be shown that $D=0$ if and only if the four nodes of the face are coplanar [13]. If $D\neq 0$,

$$\alpha=D^{-1}(\vec{a}_2\times\vec{a}_3)\cdot(\vec{x}-\vec{a}_0)\equiv f(\vec{x}), \tag{16}$$

$$\beta=D^{-1}(\vec{a}_3\times\vec{a}_1)\cdot(\vec{x}-\vec{a}_0)\equiv g(\vec{x}), \tag{17}$$

$$\alpha\beta=D^{-1}(\vec{a}_1\times\vec{a}_2)\cdot(\vec{x}-\vec{a}_0)\equiv h(\vec{x}). \tag{18}$$

Since for all points in the face $\alpha\cdot\beta=\alpha\beta$, then

$$\Phi(\vec{x})\equiv f(\vec{x})g(\vec{x})-h(\vec{x})=0, \tag{19}$$

which provides the equation of the face, or, more precisely, the equation of the surface in which the face is embedded. In this case, the so-called isoparametric mapping, Eqs. (16),(17), is linear in *x*, *y*, and *z*, while the equation of the face is nonlinear. The geometry of the surface in which a nonplanar face is embedded is discussed in Appendix A.

If D vanishes, or more practically computationally, $D\leqslant\delta_{TOL}(\Delta A)^{3/2}$, where ΔA is the area of the face and δ_{TOL} is a small dimensionless tolerance, the face is (effectively) planar. Then the vectors $\vec{a}_1\times\vec{a}_2$, $\vec{a}_2\times\vec{a}_3$ and $\vec{a}_3\times\vec{a}_1$ are (effectively) parallel (or antiparallel) to the unique face-normal vector $\hat{u}$, implying that all three of Eqs. (15) vanish identically, providing no information about α and β. In that case [14] one can take cross products of Eq. (14) with $\vec{a}_1$, $\vec{a}_2$, and $\vec{a}_3$ to obtain three equations that can be combined to give quadratic equations for α and β that have the solutions:

$$\alpha=\frac{2C}{B+\mathrm{sgn}(B)\sqrt{B^2-4AC}}, \tag{20}$$

$$\beta=\frac{2G}{F+\mathrm{sgn}(F)\sqrt{F^2-4EG}}, \tag{21}$$

where $A=\hat{u}\cdot\vec{a}_3\times\vec{a}_1$, $B=\hat{u}\cdot[\vec{a}_1\times\vec{a}_2-(\vec{x}-\vec{a}_0)\times\vec{a}_3)]$, $C=\hat{u}\cdot(\vec{x}-\vec{a}_0)\times\vec{a}_2$ and $E=\hat{u}\cdot\vec{a}_2\times\vec{a}_3$, $F=\hat{u}\cdot[\vec{a}_1\times\vec{a}_2+(\vec{x}-\vec{a}_0)\times\vec{a}_3)]$, $G=-\hat{u}\cdot(\vec{x}-\vec{a}_0)\times\vec{a}_1$. Here the equation of the face is simply

$$\Phi(\vec{x})=\hat{u}\cdot(\vec{x}-\vec{a}_0)=0, \tag{22}$$

$$\hat{u}=\frac{\vec{a}_1\times\vec{a}_2}{|\vec{a}_1\times\vec{a}_2|}, \tag{23}$$

which includes the origin if $\hat{u}\cdot\vec{a}_0=0$. Note that in this case the equation of the face is linear, but the isoparametric map, Eqs. (20),(21), is nonlinear in $\vec{x}$.

There are two cases with particular symmetry that deserve special mention. If opposite edges of a planar face are parallel, as, for example, on a regular mesh, one of the vectors $\vec{a}_2\times\vec{a}_3$, $\vec{a}_3\times\vec{a}_1$ vanishes [i.e., $\sim O(\delta_{TOL}\Delta A)$] if the face is trapezoidal, and both vanish if the face is a parallelogram, implying that one or both of A, E vanish. Then Eqs. (20), (21) reduce to

$$\alpha=\frac{C}{B}, \quad |\vec{a}_3\times\vec{a}_1|\leqslant\delta_{TOL}\Delta A, \tag{24}$$

$$\beta=\frac{G}{F}, \quad |\vec{a}_2\times\vec{a}_3|\leqslant\delta_{TOL}\Delta A. \tag{25}$$

The vector $\vec{a}_1\times\vec{a}_2$ vanishes only if the face itself has vanishing area.

2. Triangular faces

The simplest triangular face with straight edges is planar, and its representation in terms of surface coordinates inherently simpler than that of quadrilateral faces. If the nodes are at $\vec{x}^0$, $\vec{x}^1$, $\vec{x}^2$, dimensionless surface coordinates can be introduced [15] such that

$$\vec{x}=\vec{a}_0+\vec{a}_1\alpha+\vec{a}_2\beta \tag{26}$$

with

$$0\leqslant\alpha,\beta,\alpha+\beta\leqslant 1. \tag{27}$$

In the (α,β) space the face is a right triangle whose vertices are at $(\alpha,\beta)=(0,0),(0,1),(1,0)$. The coefficients in Eq. (26) are

$$\vec{a}_0=\vec{x}^0,$$

$$\vec{a}_1=\vec{x}^2-\vec{x}^0, \tag{28}$$

$$\vec{a}_2=\vec{x}^1-\vec{x}^0.$$

Taking the cross product of $\vec{a}_1$, $\vec{a}_2$ with Eq. (26) gives

$$\alpha=\frac{\hat{u}\cdot(\vec{x}-\vec{a}_0)\times\vec{a}_2}{\hat{u}\cdot\vec{a}_1\times\vec{a}_2}, \tag{29}$$

$$\beta=-\frac{\hat{u}\cdot(\vec{x}-\vec{a}_0)\times\vec{a}_1}{\hat{u}\cdot\vec{a}_1\times\vec{a}_2}, \tag{30}$$

where

$$\hat{u}=\frac{\vec{a}_1\times\vec{a}_2}{|\vec{a}_1\times\vec{a}_2|}.$$

The equation of the face is identical to that of the planar quadrilateral face, Eq. (22), the appropriate changes having been made. Note that $\vec{a}_1\times\vec{a}_2$ vanishes only for a zero-area face. For triangular faces the equation of the face as well as the isoparametric map, Eqs. (29),(30) is linear in $\vec{x}$.

B. Face-crossing detection

Given a ray's position and velocity as it enters a zone, its exit location and velocity can be determined by substituting its trajectory in the equation of each face bounding the zone and solving for the time at which the trajectory intersects the face. Thus, integration of Eq. (5) gives

$$\vec{v}(\Delta t)=\vec{v}_0-\frac{c^2}{2n_c}\langle\vec{\nabla}n_e\rangle\Delta t, \tag{31}$$

$$\vec{x}(\Delta t)=\vec{x}_0+\vec{v}_0\Delta t-\frac{c^2}{4n_c}\langle\vec{\nabla}n_e\rangle(\Delta t)^2, \tag{32}$$

where $\vec{x}_0$, $\vec{v}_0$ are the entry position and velocity. Substitution of Eq. (32) in Eq. (19) for nonplanar faces or Eq. (22) for planar faces yields a quartic or quadratic equation, respectively, to be solved for Δt. The smallest positive root [16] that, when substituted back into Eq. (32) yields a position $\vec{x}(\Delta t)$ for which α, β as calculated from Eqs. (16),(17), Eqs. (20),(21) or Eqs. (29),(30), as appropriate, satisfy the constraints (11) or (27), is the unique exit time.

C. Snell's Law

In order to apply Snell's law as a ray crosses a zonal interface the unit vector normal to the interface at the point of intersection is required. Given the equation of the surface, $\Phi(\vec{x})=0$, the unit normal is given by

$$\hat{u}=\frac{\vec{\nabla}\Phi}{|\vec{\nabla}\Phi|},$$

which is simply evaluated from Eqs. (19) or (22). To guarantee that the *outward*-pointing normal is obtained, the quantity $\hat{u}\cdot\vec{v}_{\mathrm{exit}}$, with $\vec{v}_{\mathrm{exit}}$ given by Eq. (31), is required to be positive.

As shown in Sec. II, Snell's law requires that the component of ray velocity tangent to the interface be preserved, while the component normal to the surface undergo the discontinuous change given by Eq. (6). If $\vec{v}_\perp=(\vec{v}\cdot\hat{u})\hat{u}$ and $\vec{v}_t=\vec{v}-\vec{v}_\perp$ are the normal and tangential components of the ray velocity, and unprimed (primed) quantities denote values before (after) the transition, then

$$\vec{v}\,' = \vec{v} - (\vec{v}\cdot\hat{u})\hat{u} + \sqrt{(1-n_e'/n_c)c^2 - v_t^2}\,\hat{u}. \tag{33}$$

If Eq. (6) cannot be satisfied, then the ray reflects specularly:

$$\vec{v}\,' = \vec{v} - 2(\vec{v}\cdot\hat{u})\hat{u}. \tag{34}$$

Equations (32) and (33) or Eq. (34) provide initial conditions for the ray trajectory in the next zone.

D. Grid entry

The scheme described in the previous section is guaranteed to work once the ray has entered the computational mesh. Typically, however, the beam origin is located outside the grid, necessitating a mechanism for determining the entry face. Whether or not a particular ray pierces a given boundary face can be tested by computing the vector triple product of the ray's initial velocity with the displacement from the ray origin of consecutive vertices of the face taken in cyclic order:

$$p_{ij} = \vec{v}_B\cdot(\vec{x}_{ij} - \vec{x}_B)\times(\vec{x}_{i,j+1} - \vec{x}_B), \tag{35}$$

where *i*, *j*, respectively, index the boundary face and its vertices, and $\vec{x}_B$, $\vec{v}_B$ are the ray's initial position and velocity at the beam source. If all p_{ij}'s for a given i have the same algebraic sign the ray penetrates the face; otherwise it does not. In the case of a convex boundary, two such faces will be found: entry and exit; the nearer to $\vec{x}_B$ is the entry face. If the boundary is nonconvex, more than one entry/exit pair might be found, but the face nearest the beam source will still contain the entry point. If the ray happens to come extremely close to a node or zone edge, one of the p_{ij}'s will be such that $|p_{ij}| < \delta_{RE} v_B \Delta A$, where ΔA is the area of the face being tested and δ_{RE} is a few times the machine roundoff error. In that case the criterion would be difficult to interpret and the ray would better be slightly redirected by rotation through an ''infinitesimal'' angle about a random axis. The strategy adopted for stepping through the boundary faces will clearly have a strong influence on the efficiency of the search. While serial testing of all boundary faces always works, it is inefficient. An approach based on ''bounding volumes'' [17,18] has been tested and found to greatly reduce the search time.

IV. COMPLETE RAY TRAJECTORIES

Once a ray has entered the mesh its trajectory is constructed by iterating the zone-traversal algorithm described in Sec. III B until it encounters a boundary face. This generates a piecewise continuous curve that, in general, has a directional discontinuity at each zone interface crossed. Because the error in Eq. (32) is $O(\epsilon^3)$, the composite error after N steps is $O(N\epsilon^3) \sim O(\epsilon^2) \sim O(N^{-2})$. This N^{-2} scaling is general, although in certain circumstances a high degree of symmetry in the density profile can lead to error cancellation at particular points (the test case discussed in Sec. VI B is an example of such a profile) that results in N^{-3} scaling there. In a density field with complicated structure it is possible that errors could add incoherently, leading to a $N^{-5/2}$ scaling, but lack of an analytic trajectory for comparison would make that difficult to test.

Although the accuracy of the ray trajectory is primarily determined by the linear approximation to the electron density, Eq. (1), the magnitude of a ray's group velocity is always correct (i.e., consistent with the electron density) by virtue of the motion invariant $v^2/c^2 + n_e/n_c$ built into the propagation algorithm via Snell's law.

V. POWER DEPOSITION BY INVERSE BREMSSTRAHLUNG

Because rays are simply curves in space, they carry no information about radiation intensity or spatial extent transverse to their direction. Their state is completely defined by their frequency, velocity, and power, the latter two attributes of which are, in general, spatially dependent. The power of an electromagnetic wave is depleted as the oscillatory energy it imparts to electrons is randomized by collisions, the inverse-bremsstrahlung process. The rate of energy loss is given by the well-known formula [19–21]

$$\nu_{ib} = \frac{n_e}{n_c}\nu_{ei}, \tag{36}$$

where

$$\nu_{ei} = \frac{4}{3}\left(\frac{2\pi}{m_e}\right)^{1/2}\frac{n_e Z e^4 \ln\Lambda}{T_e^{3/2}} \tag{37}$$

is the electron-ion collision rate [22]. As a ray traverses a zone its power decreases with time

$$P(\Delta t) = P(0)\exp\left\{-\int_0^{\Delta t} dt\,\nu_{ib}[\vec{x}(t)]\right\} \tag{38}$$

with $\vec{x}(t)$ given by Eq. (32), and Δt the time required to traverse the zone. Because ν_{ib} is such a strongly nonuniform function of position within a zone, care must be taken in computing the integral in Eq. (38). With Eq. (1) for $n_e[\vec{x}(t)]$ and a similar linear approximation for T_e, the integrand becomes

$$\nu_{ib}[\vec{x}(t)] = \nu_0\frac{(1+Ut+Rt^2)^2}{(1+Wt+St^2)^{3/2}}, \tag{39}$$

where

$$\begin{aligned}
U &= \frac{\vec{v}_0\cdot\langle\vec{\nabla} n_e\rangle}{n_{e0}},\\
W &= \frac{\vec{v}_0\cdot\langle\vec{\nabla} T_e\rangle}{T_{e0}},\\
R &= -\frac{c^2}{4}\frac{\langle\vec{\nabla} n_e\rangle\cdot\langle\vec{\nabla} n_e\rangle}{n_c n_{e0}},\\
S &= -\frac{c^2}{4}\frac{\langle\vec{\nabla} n_e\rangle\cdot\langle\vec{\nabla} T_e\rangle}{n_c T_{e0}}.
\end{aligned} \tag{40}$$

The quantities

$$\nu_0 \equiv \frac{4}{3}\left(\frac{2\pi}{m_e}\right)^{1/2} \frac{Ze^4}{n_c}\,\frac{n_{e0}^2 \ln \Lambda_0}{T_{e0}^{3/2}}, \tag{41}$$

$$n_{e0} \equiv \langle n_e \rangle + \langle \vec{\nabla} n_e \rangle \cdot (\vec{x}_0 - \langle \vec{x} \rangle), \tag{42}$$

$$T_{e0} \equiv \langle T_e \rangle + \langle \vec{\nabla} T_e \rangle \cdot (\vec{x}_0 - \langle \vec{x} \rangle), \tag{43}$$

and $\ln \Lambda_0$ are defined at the entry point. The integral can be evaluated in closed form, but the result is not computationally simple enough to be useful, nor warranted on accuracy grounds. A more efficient approach with sufficient accuracy is Gaussian quadrature:

$$\int_0^{\Delta t} dt\, \nu_{ib}[\vec{x}(t)] = \nu_0 \frac{\Delta t}{2} \sum_{i=1}^{N_g} w_i \frac{(1+Ut_i+Rt_i^2)^2}{(1+Wt_i+St_i^2)^{3/2}}, \tag{44}$$

where N_g is the order of the integration scheme, and w_i is the ith Gaussian weight. The evaluation times are given by $t_i = (\xi_i + 1)\Delta t/2$, with ξ_i the ith Gaussian abscissa [23]. If the integrand in Eq. (44) were known with infinite precision the quadrature error would scale as ϵ^{2N_g+1}. In fact, the truncation error in Eq. (39) due to linearly approximating n_e and T_e is $O(\epsilon^3)$, in general, so that $N_g = 2$ is acceptable. Then the integration error after N steps will be $\sim O(N\epsilon^3) \sim O(\epsilon^2) \sim O(N^{-2})$. The weak dependence of $\ln \Lambda$ on T_e can be included, if desired, by the substitution $\ln \Lambda_0 \equiv \ln \Lambda(T_{e0}) \rightarrow \ln \Lambda[T_{e0}(1+Wt+St^2)]$ [24].

The rate at which energy is deposited in the electrons in the zone is $P(0) - P(\Delta t)$, which can be used as a source term in an electron energy equation. The unattenuated ray-energy density contributes to that of the total laser field, which is discussed in Appendix B.

VI. TEST CASES

In order to check the accuracy of the ray-tracing and power deposition schemes, two test cases were designed to investigate different aspects of the algorithm. The first of these verifies that in a globally constant electron density gradient the ray-tracing scheme is exact regardless of the mesh. The second derives the scaling of the trajectory and power-deposition errors with mesh granularity in a ‘‘quadratic well’’ electron density trough.

A. Electron-density ramp on a randomized three-dimensional mesh

In this case an $(l_x \times l_y \times l_z) = (0.3 \times 0.3 \times 0.3)$ cm box was discretized on a uniform Cartesian grid of $20 \times 1 \times 20$ zones. The grid was then deformed by imposing random three-dimensional perturbations on all nodes (except those in the $x = 0, l_x$ and $z = 0, l_z$ planes) of r.m.s. magnitude $\approx 0.25 \times 0.3/20$ cm (i.e., about 25% of the nominal grid spacing). All internal faces of the resulting mesh were nonplanar, and thus required the use of the most complicated level of the interface-crossing algorithm, Eqs. (16)–(19) with Eqs. (31), (32). An electron density profile with uniform density gradient $\vec{\nabla} n_e = (5/2) n_c (\hat{e}_x + \hat{e}_z)$ was laid down on the perturbed mesh, which consequently included part of the critical surface $x + z = 0.4$, where $\omega_p(x,z) = \omega$. Rays were launched from points below the mesh $(0 < x < l_x, 0 < y < l_y, z < 0)$, in the z direction and followed through the mesh until they reached a boundary face. Because the spatial variation of the electron density was linear, Eq. (1) was exactly satisfied, implying that there were no density-discontinuities at zone interfaces. Consequently, Snell's law produced no discontinuous changes in ray direction: the ray paths were exactly parabolic, and were found to agree with analytic solutions of Eq. (5) to within machine roundoff. The trajectory of a typical ray is shown in Fig. 1.

B. Electron-density quadratic trough

To check the scaling of trajectory and power-deposition errors with the mesh spacing when the electron density gradient is not constant, a test case was designed for which the ray equation of motion Eq. (5) could be solved and the integral in Eq. (38) evaluated analytically for comparison with the numerical results. A ‘‘quadratic trough’’ electron density profile

$$n_e(\vec{x}) = n_w + (n_c - n_w)\left(\frac{z - z_w}{z_c - z_w}\right)^2, \tag{45}$$

was laid down on a one-dimensional $(1 \times 1 \times N_z)$-zone uniform grid with $0 \leqslant x \leqslant l_x = 0.1$ cm, $0 \leqslant y \leqslant l_y$, $0 \leqslant z \leqslant l_z = 10$ cm. The planes $z = 0$ and $z = 10$ cm were critical surfaces, and $n_w = n_c/2$ the electron density at the bottom of the trough, located at $z_w = 5$ cm. The edges of the N_z zones were at $Z_k = k l_z / N_z$, $k = 0, 1, \ldots, N_z$. The density in zone k was taken to be $\langle n_e \rangle_k = [n_e(Z_{k+1}) + n_e(Z_k)]/2$, while the density gradient in the zone was $\langle \vec{\nabla} n_e \rangle_k = \hat{e}_z(\langle n_e \rangle_{k+1} - \langle n_e \rangle_{k-1})/(2\Delta z)$. (Ghost zones were used to compute $\langle \vec{\nabla} n_e \rangle_k$ for $k = 1, N_z$.)

As a ray propagates along the density channel and across the density gradient at constant $v_y = v_{y0} = c\sqrt{1 - n_e(z_0)/n_c}$, it oscillates in z between turning points at $z = z_0$ and $z = 2z_w - z_0$. With initial conditions

$$\vec{x}(0) = (x_0, 0, z_0),$$

$$\vec{v}(0) = (0, v_{y0}, 0),$$

the equation of motion (5) with Eq. (45) has the exact solution

$$x(t) = x_0,$$

$$y(t) = v_{y0} t,$$

$$z(t) = z_w + (z_0 - z_w)\cos\left(\frac{2\pi t}{\tau}\right),$$

where $\tau = (2\pi/c)(z_c - z_w)/\sqrt{1 - n_w/n_c}$ is the period of the motion. Upon elimination of t

$$z(y) = z_w + (z_0 - z_w)\cos\left(\frac{2\pi y}{v_{y0}\tau}\right). \tag{46}$$

A plot of one wavelength of the motion, $0 \leqslant y \leqslant v_{y0}\tau = 8\pi$, is shown superimposed on a contour plot of the electron

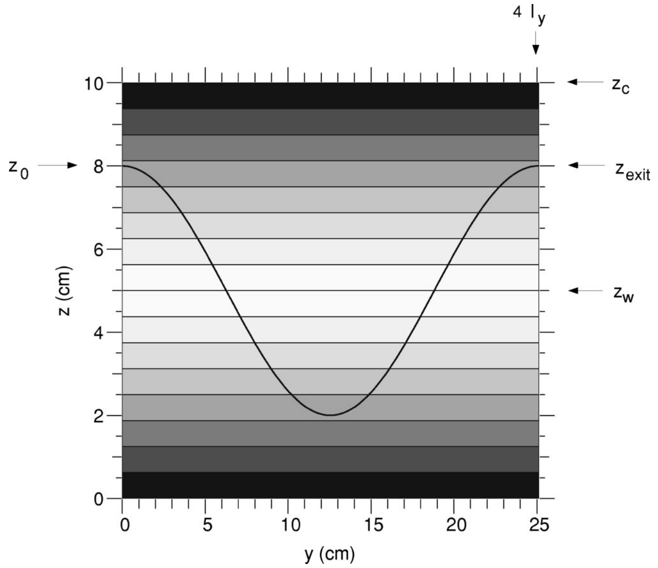

FIG. 2. One wavelength of the analytic ray trajectory given by Eq. (46), superimposed on a contour plot of the electron density trough, Eq. (45). A case with $N_z = 16$ is shown, with $\langle n_e \rangle$ indicated by the gray scale. At this scale an overlay of the numerical trajectory would be visually indistinguishable from the analytic one.

density trough in Fig. 2. To investigate error scaling, the length of the grid in the y direction was chosen to be one quarter-wavelength of the motion [25]:

$$l_y = v_{y0}\tau/4 = (\pi/2)\sqrt{(z_c - z_w)^2 - (z_0 - z_w)^2}$$

(which, remarkably, is independent of the electron density). Thus the analytic trajectory leaves the grid at $\vec{x}_{\rm exit}^{\rm an} = (x_0, l_y, z_w)$. The numerical trajectory that results from applying the ray propagation scheme of Secs. II and III to the same initial conditions leads to an exit point $\vec{x}_{\rm exit}^{\rm num} = (x_0, l_y, z_{\rm exit})$, which, in general, differs from $\vec{x}_{\rm exit}^{\rm an}$ by an error δz that depends on the resolution of the grid. The scaling of this error is shown in Fig. 3(a), which plots $\epsilon_T \equiv |\delta z|/2(z_0 - z_w)$ as a function of N_z for a ray with $x_0 = 0.05$ cm, $z_0 = 8$ cm. The observed variation of the error with the mesh is consistent with $\epsilon_T \propto N_z^{-2}$, in agreement with the error analysis in Sec. IV. The motion invariant $v^2/c^2 + n_e/n_c$ [recall Eq. (7)] maintained a constant value of unity to within machine roundoff.

To check the power deposition scheme, an electron temperature profile was chosen to give a damping rate for which the integral in Eq.(38) could be evaluated analytically. In particular,

$$T_e(\vec{x}) = T_w[n_e(\vec{x})/n_w]^{2/3}, \qquad (47)$$

(T_w is the temperature at the bottom of the trough) which makes $\nu_{ib} \propto n_e[\vec{x}(t)]$, giving [26]

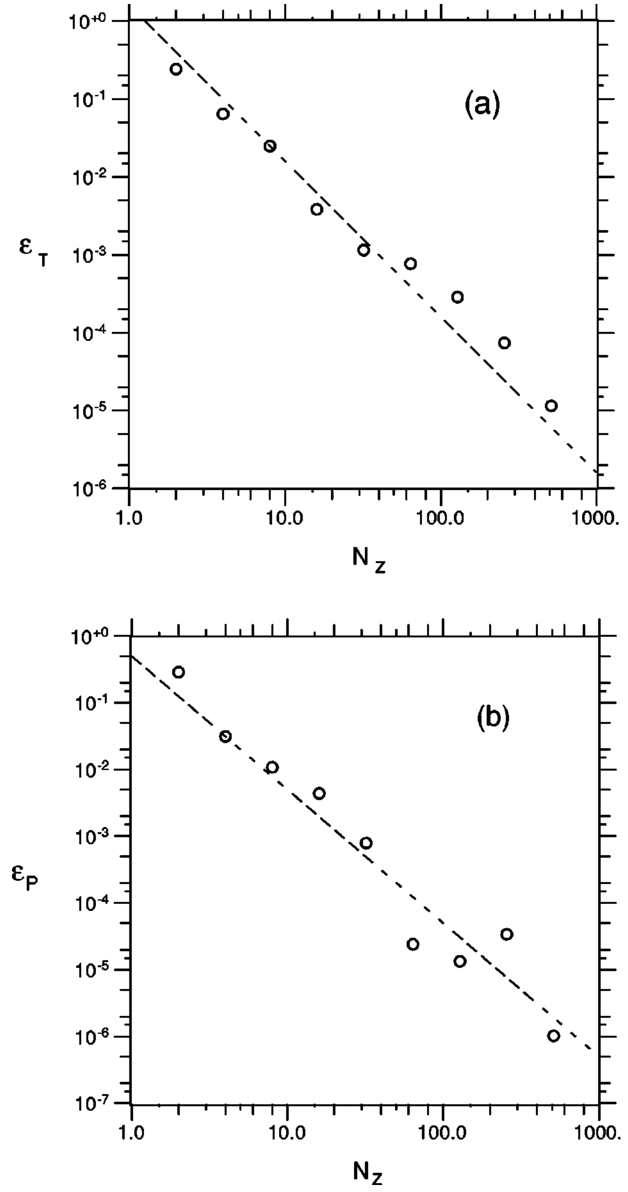

FIG. 3. Dimensionless errors in the electron-density-trough test case: (a) Trajectory error at the exit point as a function of the number of zones. The slope of the dashed line is $d \log \epsilon_T / d \log N_z = -2$; (b) Relative error in deposited power as a function of the number of zones. The slope of the dashed line is $d \log \epsilon_P / d \log N_z = -2$.

$$\begin{aligned} \int_0^{\tau/4} dt\, \nu_{ib}[\vec{x}(t)] &= \nu_w \int_0^{\tau/4} dt \Bigg[1 + \frac{n_c - n_w}{n_w} \\ &\qquad \times \left(\frac{z_0 - z_w}{z_c - z_w} \right)^2 \cos^2\!\left(\frac{2\pi t}{\tau} \right) \Bigg] \\ &= \nu_w \frac{\tau}{4} \left[1 + \frac{1}{2} \frac{n_c - n_w}{n_w} \left(\frac{z_0 - z_w}{z_c - z_w} \right)^2 \right], \end{aligned} \qquad (48)$$

where ν_w is the inverse-bremsstrahlung rate at the bottom of the trough. For the same ray and density profile used to obtain the trajectory-error scaling, and with $T_w = 10$ keV, Eq.

(48) gives $P_{\rm dep}\equiv P(0)-P(\tau/4)=(0.433\dots)P(0)$ for the total power deposited. The fractional error in the deposited power, $\epsilon_P\equiv|P^{\rm num}_{\rm dep}-P^{\rm an}_{\rm dep}|/P^{\rm an}_{\rm dep}$, with $P^{\rm num}_{\rm dep}$ given by Eq. (44), is shown in Fig. 3(b). It was observed to scale as N_z^{-2}, consistent with the analysis in Sec. V.

The trajectory and power deposition errors at subsequent crossings of the trough bottom ($t=3\tau/4, 5\tau/4$) were also checked. While larger in magnitude than those at $t=\tau/4$, the scaling was again $\sim N_z^{-2}$.

VII. SUMMARY AND DISCUSSION

A scheme for modeling propagation and absorption of laser light in a transparent medium with a spatially varying index of refraction has been presented. Based on the geometrical-optics limit of the full electromagnetic wave equation, it follows rays through an unstructured three-dimensional mesh on which they deposit power absorbed by the inverse-bremsstrahlung process. Ray trajectories are obtained by solving the ray equation of motion, in which the electron number density is shown to play the role of an effective potential. The spatial variation of the electron density within a computational zone is modeled with a linear approximation based on the ratio of the zone size to the density-gradient scale length ϵ as a small parameter. This leads to a parabolic intrazone ray path that includes refractive effects and is correct to $O(\epsilon^2)$. In general, the approximation also leads to density discontinuities at zone interfaces that must be accommodated by application of Snell's law. Zone interfaces may be triangular or quadrilateral. The former are assumed planar, the latter are, in general, nonplanar. By assuming a quadrilateral face to have a bilinear representation in terms of two-dimensional surface coordinates, an equation for the three-dimensional surface in which it is embedded is derived. The time and location at which a ray exits a zone are determined by substituting the equation of motion into the appropriate face equation. The basic zone-traversal/interface-transition scheme is iterated to generate the complete ray trajectory, whose error is $O(\epsilon^2)$. The amount of power deposited as a ray crosses a zone is computed by integrating the inverse-bremsstrahlung absorption rate along the ray path using Gaussian quadrature to capture the structure of the highly nonuniform deposition rate ($\propto n_e^2/T_e^{3/2}$). The error in the total amount of power deposited on the mesh is, again, $O(\epsilon^2)$.

The propagation-deposition scheme applies directly to meshes made up of hexahedra, prisms, pyramids, and tetrahedra. Zones with faces of more than four edges would require decomposition of such faces into quadrilateral or triangular subfaces, or subdivision of such zones into those of the four allowable types.

Test cases were presented to demonstrate that (1) in a constant electron-density-gradient the scheme obtains ray trajectories that are exact to within roundoff on a randomized three-dimensional hexahedral mesh; (2) in a quadratic electron-density trough ray trajectories and energy-deposition rates are obtained whose error scaling is $O(\epsilon^2)$, in agreement with that predicted.

The laser propagation-deposition scheme developed in this paper has obvious directions for extension. For example, a much simpler form, in which there is no need for refraction and a different power-deposition formula is used would apply to charged-particle drivers. The basic method could also be easily adapted to other types of computational mesh, either simpler types like a structured hexahedral, or more complicated types like an arbitrary polyhedral. Additional physics like ponderomotive effects and resonant absorption could be added without difficulty. A more significant upgrade would address diffractive effects by quasioptical techniques [5,6].

ACKNOWLEDGMENTS

I am especially grateful to Jose Milovich and Gary Kerbel for their help in implementing and testing the ray-tracing and power deposition scheme. Thanks are due also to Alex Friedman for access to unpublished work, and to Jack Byers, Bruce Cohen, Steve Langer, Manoj Prasad, Alek Shestakov and George Zimmerman for many helpful discussions. This work was performed under the auspices of the U. S. D. O. E. by the Lawrence Livermore National Laboratory under Contract No. W-7405-ENG-48.

APPENDIX A: GEOMETRY OF QUADRILATERAL FACES

In order to more easily visualize the intersection of rays with a nonplanar quadrilateral face, i.e., one for which the quantity $D=\vec{a}_1\cdot(\vec{a}_2\times\vec{a}_3)$ is nonvanishing, it is useful to study the geometry of such faces in some detail. The surface in which the face is embedded satisfies Eq. (19). Its intersection with a coordinate plane ($x_i=\text{const}$, $i=1,2,3$) is an unbounded conic section, i.e., a hyperbola or a parabola; the entire surface is a hyperbolic paraboloid. To demonstrate this it is sufficient to concentrate on the quadratic terms in Φ. In terms of the relative coordinates, $\vec{\rho}\equiv\vec{x}-\vec{a}_0$, the quadratic part of Φ is the quadratic form

$$\Phi_2\equiv\left(\frac{\vec{a}_2\times\vec{a}_3}{D}\cdot\vec{\rho}\right)\left(\frac{\vec{a}_3\times\vec{a}_1}{D}\cdot\vec{\rho}\right)=\vec{\rho}\cdot\mathbf{Q}\cdot\vec{\rho}, \tag{A1}$$

where the matrix $\mathbf{Q}$ is the dyadic product of $\vec{a}_2\times\vec{a}_3/D$ and $\vec{a}_3\times\vec{a}_1/D$, and the vectors $\vec{a}_i$ are defined in Eqs. (13). The intersection of the surface with any of the coordinate planes $\rho_i=\text{const}$ is a curve whose nature is determined by its *discriminant*, a function of the coefficients of the quadratic terms in Φ_2 involving the nonconstant coordinates. For example, if ρ_1 is constant, the discriminant of the relevant terms in Φ_2, viz., $\mathbf{Q}_{22}\rho_2^2+(\mathbf{Q}_{23}+\mathbf{Q}_{32})\rho_2\rho_3+\mathbf{Q}_{33}\rho_3^2$ is

$$\Delta_1=(\mathbf{Q}_{23}+\mathbf{Q}_{32})^2-4\mathbf{Q}_{22}\mathbf{Q}_{33},$$

and similarly for ρ_2 and ρ_3:

$$\Delta_2=(\mathbf{Q}_{13}+\mathbf{Q}_{31})^2-4\mathbf{Q}_{11}\mathbf{Q}_{33},$$

$$\Delta_3=(\mathbf{Q}_{12}+\mathbf{Q}_{21})^2-4\mathbf{Q}_{11}\mathbf{Q}_{22}.$$

Now $\mathbf{Q}_{ij}$ is

$$\mathbf{Q}_{ij}=\left[\frac{\vec{a}_2\times\vec{a}_3}{D}\right]_i\left[\frac{\vec{a}_3\times\vec{a}_1}{D}\right]_j$$

so that $\mathbf{Q}_{ij}\mathbf{Q}_{ji}=\mathbf{Q}_{ii}\mathbf{Q}_{jj}$, implying

$$\Delta_k=(\mathbf{Q}_{ij}-\mathbf{Q}_{ji})^2\geqslant 0, \quad i\neq j\neq k\neq i.$$

The curve formed by the intersection of the surface with coordinate plane $\rho_k=\text{const}$ is a hyperbola if $\Delta_k>0$, a parabola if $\Delta_k=0$; in either case it is unbounded. In terms of the vectors $\vec{a}_i$, the discriminant Δ_k is

$$\Delta_k=\left[\hat{e}_k\cdot\left(\frac{\vec{a}_2\times\vec{a}_3}{D}\right)\times\left(\frac{\vec{a}_3\times\vec{a}_1}{D}\right)\right]^2,$$

where $\hat{e}_k$ is a unit vector in the ρ_k direction. Expansion of the cross products gives

$$\Delta_k=\left(\frac{\hat{e}_k\cdot\vec{a}_3}{D}\right)^2.$$

Thus we have the simple result that if any component of $\vec{a}_3$ vanishes, the curve formed by the intersection of the surface with the corresponding coordinate plane is parabolic; otherwise it is a hyperbola. Since it is always possible to rigidly rotate the face (or, equivalently, the coordinate frame) to align $\vec{a}_3$ with a coordinate axis, there is some coordinate system in which the intersection of the surface with the corresponding coordinate plane is hyperbolic, and with the other two coordinate planes parabolic. In other words, the three-dimensional surface in which the face is embedded is a hyperbolic paraboloid [27]. For example, if $\vec{a}_3$ is along the ρ_1 axis, with suitable coordinate scaling the equation of the surface can be cast in the standard form $\Phi=\rho_1-\rho_2^2+\rho_3^2=0$.

The surface coordinates α and β span the entire surface. That segment of the surface that is coincident with the quadrilateral face under consideration is determined by the condition (11). Thus, although an arbitrary parabolic ray trajectory might intersect the *surface* as many as four times [substitution of Eq. (32) in Eq. (19) yields a quartic equation for the exit time], only those intersections satisfying the constraints on α and β need be considered as possible exit points in the face. For faces that are only slightly nonplanar $(D\to 0)$ the distance between surface intersection points can be quite small, necessitating high accuracy in solving for candidate exit times [28]. For example, it is straightforward to show from Eq. (19) that for a ray intersecting such a face at $\vec{x}=\vec{a}_0$ $(\Rightarrow\alpha=\beta=0)$ and oriented parallel to $\vec{a}_1\times\vec{a}_2$, there is another point where the ray intersects the surface (but not the *face*) separated from $\vec{a}_0$ by a distance that scales as $D/\Delta A$, where ΔA is the area of the face. Thus, as the face approaches planarity $(D\to 0)$ two intersection points become arbitrarily close. Because $\vec{\nabla}\alpha$ and $\vec{\nabla}\beta$ scale as D^{-1}, however, the variation in α and β from one intersection point to the other remains finite, and in fact exceeds unity, making determination of the true exit point unambiguous as long as the intersection times are computed with sufficient accuracy.

An example is depicted in Fig. 4, where a quadrilateral face specified by the nodes $\vec{x}^n=\{(0,0,0),(1,0,0),(1.5,1.5,-\zeta),(0,1,0)\}$, $\zeta=0.25$, as well as part of the embedding surface $\Phi(\vec{x})=0$, is shown. The face (emphasized grid lines) corresponds to $-1\leqslant\alpha,\beta\leqslant 1$, while the segment of the surface shown is for $-7\leqslant\alpha,\beta\leqslant 1$. Note that the grid lines, along which either α or β is constant, are straight. The dimensionless "nonplanarity" parameter for the face is $|D|/\Delta A^{3/2}=8.4\times 10^{-3}$. If ζ were smaller, i.e., the face were more nearly planar, $|D|$ would be smaller, and the distance between the upper and lower sheets of the surface, which scales with $|D|$, would be smaller. Thus, for example, a ray that was approximately straight and parallel to the z axis that penetrated the face also would cross the lower sheet, the distance between intersection points going to zero with $|D|$.

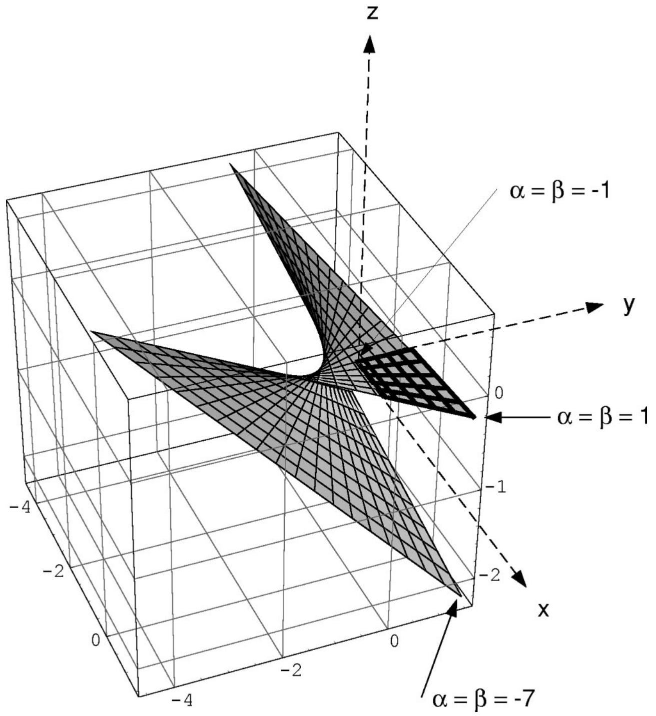

FIG. 4. A nonplanar quadrilateral face (emphasized grid lines) and its embedding hyperbolic paraboloid. Along grid lines either α or β is constant. The unit of the Cartesian coordinates $\{x,y,z\}$ is cm, while $\{\alpha,\beta\}$ are dimensionless.

APPENDIX B: LASER-FIELD ENERGY DENSITY

In addition to providing a source for electron energy transport, the laser-plasma interaction model can also furnish a momentum source by way of ponderomotive effects, which depend on the laser-field energy density and its gradient [29,30]. The contribution of a single ray to the energy density of the laser field in a zone can be computed as $\mathcal{E}_R=\langle P\rangle\Delta t/\Delta V$, where Δt is the time it takes the ray to cross the zone and ΔV is the zone volume. Taking $\langle P\rangle$ to be given by the time-averaged power

$$\langle P\rangle=\frac{1}{\Delta t}\int_0^{\Delta t}dt\,P(t)$$

with $P(t)$ given by Eqs. (38),(44), one finds, using the trapezoidal rule, to $O[\epsilon(\nu_{ib}\Delta t)+(\nu_{ib}\Delta t)^2]$,

$$\mathcal{E}_R=\frac{P(0)+P(\Delta t)}{2}\,\frac{\Delta t}{\Delta V}. \tag{B1}$$

Higher-order terms could, of course, be kept if desired by using a higher-order integration scheme to evaluate $\langle P \rangle$. The advantage of Eq. (B1) is that $P(0)$ and $P(\Delta t)$ are already known from the power deposition calculation. The total laser-field energy density in a zone $\mathcal{E}_L$ is obtained by summing Eq. (B1) over all rays that visit the zone in a given time step [31]: $\mathcal{E}_L = \Sigma_R \mathcal{E}_R$. The jitter velocity v_{osc} of electrons in the laser electric field is related to the total laser-field energy density [19] by $\mathcal{E}_L = (1/2) n_c m_e \langle v_{\mathrm{osc}}^2 \rangle$. A convenient measure of the strength of the laser field is given by the ratio $\langle (v_{\mathrm{osc}}/v_e)^2 \rangle = \mathcal{E}_L / n_e T_e$, where v_e is the electron thermal velocity and T_e is the electron temperature.

[1] D. S. Kershaw, M. K. Prasad, M. J. Shaw, and J. L. Milovich, Comput. Methods Appl. Mech. Eng. **158**, 81 (1997).

[2] A. I. Shestakov, M. K. Prasad, J. L. Milovich, N. A. Gentile, J. F. Painter, and G. Furnish, *ICF Quarterly Report*, Lawrence Livermore National Laboratory, Livermore, CA, UCRL-LR-105821-96-6, Vol. 6, No. 4, July-Sep. 1996, pp. 165–180.

[3] A. I. Shestakov, J. Milovich, and D. Kershaw, SIAM News, **32**(4), 6 (1999). This paper presents results of a parallelized simulation of a laser-driven 3D implosion that uses the scheme developed in the present paper.

[4] D. S. Miller (private communication) on KULL, an LLNL ASCI code being developed to perform ICF simulations.

[5] E. Mazzucato, Phys. Fluids B **1**, 1855 (1989).

[6] G. V. Pereverzev, Nucl. Fusion **20**, 109 (1992).

[7] A. Friedman, Bull. Am. Phys. Soc. **28**, 1124 (1983).

[8] In general, more than one way exists to compute $\langle \vec{\nabla} n_e \rangle$ from the available data. Care must always be taken that the method chosen satisfies crucial constraints, e.g., that n_e computed by Eq. (1) be non-negative.

[9] L. D. Landau and E. M. Lifshitz, *Electrodynamics of Continuous Media* (Addison-Wesley, Reading, MA, 1966).

[10] G. Zimmerman (private communication).

[11] L. Lapidus and G. F. Pinder, *Numerical Solution of Partial Differential Equations in Science and Engineering* (Wiley, New York, 1982), Chap. 3.

[12] The order of the nodes is important: each unique ordering determines a different surface.

[13] That coplanarity implies $D=0$ is clear. To prove the converse, define $\vec{\xi}^n \equiv \vec{x}^n - \vec{x}^0$. Then $D = \vec{\xi}^2 \cdot (\vec{\xi}^3 \times \vec{\xi}^1)/16$, from which it is obvious that $D=0$ implies that $\vec{\xi}^2$ can have no component parallel to $\vec{\xi}^3 \times \vec{\xi}^1$, i.e., either $\vec{\xi}^1$, $\vec{\xi}^2$, and $\vec{\xi}^3$ (the displacements of nodes 1, 2, and 3 from node 0) are coplanar, or one of them vanishes, in which case two nodes coincide.

[14] Nothing in the derivation of Eqs. (20),(21) depends on $D=0$ so that those equations are also applicable to the nonplanar case. Equations (16),(17) are simpler to compute, however, and therefore preferable.

[15] Jose Milovich (private communication).

[16] In practice, the smallest root larger than $\delta_{RE}(\Delta V)^{1/3}/c$, where δ_{RE} is a few times the machine roundoff error, ΔV is the zone volume, and c is the speed of light, would be used.

[17] Gary Kerbel (private communication).

[18] Nicholas Wilt, *Object-Oriented Ray Tracing in C++* (Wiley, New York, 1994).

[19] W. L. Kruer, *The Physics of Laser Plasma Interactions* (Addison-Wesley, Redwood City, CA, 1988).

[20] D. L. Book, NRL Plasma Formulary, NRL Publication 0084-4040, 1986.

[21] T. W. Johnston and J. M. Dawson, Phys. Fluids **16**, 722 (1973).

[22] S. I. Braginskii, in *Reviews of Plasma Physics*, edited by M. A. Leontovich (Consultants Bureau, New York, 1965), Vol. 1, p. 205.

[23] *Handbook of Mathematical Functions with Formulas, Graphs, and Mathematical Tables*, edited by M. Abramowitz and I. A. Stegun (Wiley, New York, 1972), Sec. 25.4.30.

[24] The Coulomb logarithm is independent of n_e in the presence of a laser electric field [19–21].

[25] Due to the periodic nature of the ray motion, there is a fortuitous cancellation of accumulated trajectory error each time the ray reaches a point that is an integral number of half-wavelengths from its starting point that leads to an apparent error scaling $\sim N^{-3}$. Conversely, the error is largest at odd numbers of quarter-wavelengths from the starting point and scales as expected there.

[26] For simplicity $\ln \Lambda$ was fixed at its value at $z = z_w$.

[27] The same result can be derived from a more lengthy algebraic analysis of all the coefficients of $\Phi(\vec{x})$. See W. H. Beyer, *CRC Standard Mathematical Tables*, 28th ed. (CRC, Boca Raton, FL, 1989), pp. 210–211.

[28] Gary Kerbel (private communication).

[29] J. J. Thompson, C. E. Max, and K. Estabrook, Phys. Rev. Lett. **35**, 663 (1975).

[30] J. Harte and G. Zimmerman, LLNL Report UCRL 79860, 1978.

[31] Note that summing individual ray energy densities presupposes that the rays are statistically independent.